STRUCTURAL BIOLOGY COMMUNICATIONS

ISSN 2053-230X

Received 12 December 2025
Accepted 26 January 2026

Edited by A. Nakagawa, Osaka University, Japan

Keywords: monobodies; aggregation; maltose-binding protein; fusion-protein crystallization; *in situ* X-ray diffraction.

PDB reference: Mb-P′-1, 21dh

Supporting information: this article has supporting information at journals.iucr.org/f

Crystallization and X-ray structure of a highly aggregation-prone monobody engineered for high-affinity small-molecule recognition

Koushirou Endo,[a] Shun Umemoto,[b] Nariaki Tsuzuki,[b] Hideo Okumura,[c] Yusuke Sato,[a,d,e] Tatsuyuki Yoshii,[f,g] Shinya Tsukiji,[f,h] Shingo Nagano,[a,d] Hiroshi Murakami[b,i,j]* and Tomoya Hino[a,d,e]*

[a]Department of Chemistry and Biotechnology, Graduate School of Engineering, Tottori University, 4-101 Koyamacho-minami, Tottori, Tottori 680-8552, Japan, [b]Department of Biomolecular Engineering, Graduate School of Engineering, Nagoya University, Furo-cho, Chikusa-ku, Nagoya, Aichi 464-8601, Japan, [c]Diffraction and Scattering Division, Japan Synchrotron Radiation Research Institute, 1-1-1 Kouto, Sayo-cho, Sayo-gun, Hyogo 679-5198, Japan, [d]Center for Research on Green Sustainable Chemistry, Tottori University, 4-101 Koyamacho-minami, Tottori, Tottori 680-8552, Japan, [e]Chromosome Engineering Research Center, Tottori University, 86 Nishi-cho, Yonago, Tottori 683-8503, Japan, [f]Department of Life Science and Applied Chemistry, Nagoya Institute of Technology, Gokiso-cho, Showa-ku, Nagoya, Aichi 466-8555, Japan, [g]PRESTO, Japan Science and Technology Agency (JST), Kawaguchi, Saitama 332-0012, Japan, [h]Department of Nanopharmaceutical Sciences, Nagoya Institute of Technology, Gokiso-cho, Showa-ku, Nagoya, Aichi 466-8555, Japan, [i]Institute of Nano-Life-Systems, Institutes of Innovation for Future Society, Nagoya University, Furo-cho, Chikusa-ku, Nagoya, Aichi 464-8601, Japan, and [j]Research Institute for Quantum and Chemical Innovation, Institutes of Innovation for Future Society, Nagoya University, Furo-cho, Chikusa-ku, Nagoya, Aichi 464-8601, Japan. *Correspondence e-mail: murah@chembio.nagoya-u.ac.jp, t_hino@tottori-u.ac.jp

Monobodies, engineered protein scaffolds derived from the fibronectin type III domain, are powerful alternatives to conventional antibodies. While the native scaffold is robust, engineering the variable loops can often compromise solubility and promote aggregation. Here, we report the crystallization and structure determination at 2.57 Å resolution of a monobody (Mb-P′) engineered to bind the synthetic small molecule HPPU [1-(4-hydroxyphenyl)-3-phenylurea] with nanomolar affinity. Although Mb-P′ exhibited severe polydispersity and heterogeneous oligomerization in solution, N-terminal fusion with maltose-binding protein (MBP) using an optimized linker successfully yielded monodisperse species and diffraction-quality crystals. The crystal structure exhibited pseudo-D_3 symmetry in the asymmetric unit, in which the MBP moiety interacts with and partially covers the F and G β-strands of the monobody. This steric masking suggests that MBP acts as a solubility enhancer by shielding the aggregation-prone surface patches generated by loop engineering. Our results demonstrate that this fusion strategy effectively enables structural studies of aggregation-prone proteins obtained from engineered scaffolds.

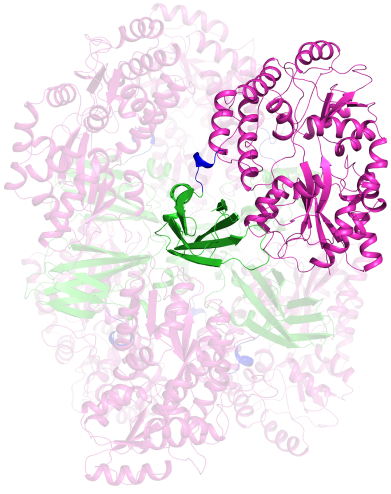

1. Introduction

The precise characterization of protein–small molecule interactions is essential for advancing drug discovery and the development of efficient protein-based recognition systems. Conventional antibodies frequently exhibit high-affinity and highly specific binding to small molecules, including haptens and other low-molecular-weight ligands. This specificity arises from structurally complex variable regions that form multiple contacts through hydrophobic, aromatic and hydrogen-bonding interactions, enabling the recognition of diverse chemical scaffolds. However, the development and production of conventional antibodies for small-molecule targets often requires extensive optimization, involving time-consuming immunization protocols and costly screening procedures.

By contrast, smaller antibody fragments or synthetic protein scaffolds, such as single-domain antibodies (VHHs or nanobodies; Hamers-Casterman *et al.*, 1993; Muyldermans *et al.*,

1994), monobodies (Koide *et al.*, 1998; Batori *et al.*, 2002) and DARPins (Binz *et al.*, 2003; Binz *et al.*, 2004), generally display simpler architectures and offer distinct advantages including enhanced stability and simplified production. While these scaffolds can be engineered to bind proteins with high affinity, there are only limited examples where these scaffolds bind small molecules with high affinity (Bever *et al.*, 2016).

Monobodies, which are derived from the fibronectin type III (FN3) domain, have emerged as versatile scaffolds owing to their stability, small size (∼10 kDa) and the high degree of freedom in loop design. They have been widely applied in functional analysis and intracellular inhibition, and as powerful tools in structural biology, with 97 crystal structures now deposited in the Protein Data Bank. The development of advanced library design strategies, including 'side-and-loop' approaches that utilize β-sheet surfaces for concave binding interfaces, has significantly expanded the potential applications of monobodies beyond traditional protein–protein interactions (Koide *et al.*, 2012).

Despite these advances, structural and thermodynamic studies of monobodies binding to small molecules with high affinity remain scarce. Recently, we isolated a high-affinity monobody (Mb-P′) against the synthetic small molecule 1-(4-hydroxyphenyl)-3-phenylurea (HPPU; Fig. 1) using TRAP display technology (Ishizawa *et al.*, 2013; Kondo *et al.*, 2021). However, structural characterization of Mb-P′ was hindered by its tendency to form heterogeneous oligomers in solution, a common bottleneck in the development of engineered scaffolds.

To overcome this aggregation problem, we employed a crystallization chaperone strategy using maltose-binding protein (MBP) fusion (Center *et al.*, 1998). By optimizing the inter-domain linker, we successfully crystallized and determined the structure of the Mb-P′–HPPU complex at high resolution. Structural analysis further reveals that MBP contributes to stabilization by sterically masking the aggregation-prone F and G β-strands. These findings highlight MBP fusion as an effective and generalizable approach to enable crystallographic studies of engineered binding proteins that are otherwise difficult to crystallize.

2. Materials and methods

2.1. Macromolecule production

The gene encoding the monobody Mb-P′ was cloned into the bacterial expression vector pQ107, which utilizes a T5 promoter, to produce a protein bearing an N-terminal His_6 tag. However, since the nickel-purified protein exhibited severe aggregation (Fig. 2*a*), we adopted an MBP fusion strategy to facilitate monomerization. For this construct, Mb-P′ was cloned into pET-28b(+) for fusion with an N-terminal MBP variant (N393A; derived from pMALc4X). To optimize the construct for crystallization, two different inter-domain linkers were evaluated: NAAATGS and TSGTGS. The NAAA sequence motif is commonly used in structural studies of MBP-fusion proteins for its favorable crystallization properties (Waugh, 2016) and the TGS extension provides conformational flexibility at the MBP–monobody junction. The alternative TSGTGS linker was designed *de novo* in this

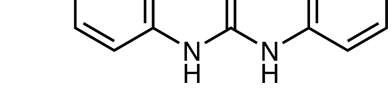

Figure 1
Chemical structure of HPPU.

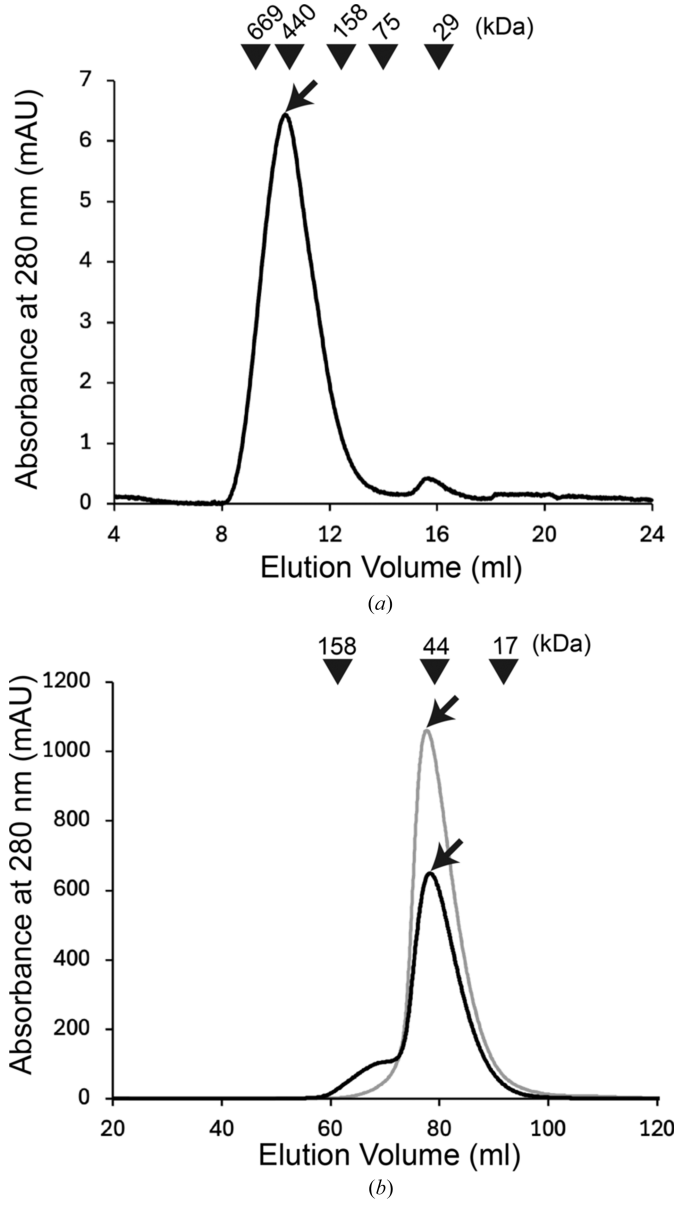

Figure 2
Gel-filtration chromatography profiles of two MBP-fused Mb-P′ constructs. (*a*) Gel-filtration profile of Mb-P′ expressed without an MBP fusion. (*b*) Gel-filtration profiles of MBP–Mb-P′ fusion constructs carrying different MBP–monobody linker sequences: NAAATGS (black) and TSGTGS (gray). In both panels, inverted triangles indicate the elution positions of molecular-mass standards. Arrows indicate the elution peaks corresponding to the Mb-P′ protein in (*a*) and the MBP–Mb-P′ fusion proteins in (*b*).

Table 1
Macromolecule-production information.

Protein	His-tagged Mb-P′	Mb-P′-1	Mb-P′-2
DNA source	Synthetic gene	Synthetic gene	Synthetic gene
Amino-acid length	155	487	486
Molecular weight (Da)	13341	53840	53785
Expression vector	pQ107	pET-28b(+)	pET-28b(+)
N-terminal tag	His_6	MBP (N393A)	MBP (N393A)
Linker sequence	None	NAAATGS	TSGTGS
Expression host	*E. coli* BL21(DE3)	*E. coli* BL21(DE3)	*E. coli* BL21(DE3)

work; it is one residue shorter to reduce junctional flexibility and was enriched in polar residues to increase hydrophilicity and mitigate aggregation.

The expression vectors for Mb-P′-1 (NAAATGS linker) and Mb-P′-2 (TSGTGS linker) were transformed into *Escherichia coli* BL21(DE3). Cells were grown in LB medium containing kanamycin at 37°C until the optical density at 600 nm reached 0.5. Protein expression was induced with 0.5 m*M* isopropyl *β*-D-1-thiogalactopyranoside, followed by incubation at 25°C for 16 h.

Cells were harvested by centrifugation at 6000 rev min^{-1} for 10 min and resuspended in lysis buffer [50 m*M* Tris–HCl pH 8.0, 0.3 *M* NaCl, 10%(*v*/*v*) glycerol, 0.5 mg ml^{-1} lysozyme, 0.1 mg ml^{-1} in-house-prepared recombinant *Serratia marcescens* nuclease, 1 m*M* phenylmethylsulfonyl fluoride, 1%(*v*/*v*) Triton X-100] at a ratio of 6 ml per gram of wet cell pellet. After stirring for 1 h at room temperature, the cells were disrupted by sonication and the lysate was clarified by centrifugation at 10 000*g* for 30 min.

The supernatant was applied onto an amylose resin column (New England Biolabs) pre-equilibrated with wash buffer I (50 m*M* Tris–HCl pH 8.0, 0.3 *M* NaCl, 10% glycerol, 1% Triton X-100). The column was washed sequentially with 10 CV of wash buffer I and 10 CV of wash buffer II (50 m*M* Tris–HCl pH 8.0, 0.3 *M* NaCl, 10% glycerol). Bound proteins were eluted with elution buffer (50 m*M* Tris–HCl pH 8.0, 0.3 *M* NaCl, 10% glycerol, 20 m*M* maltose). The eluate was concentrated to ∼10 mg ml^{-1} using Amicon Ultra-15 centrifugal filters (30 kDa molecular-weight cutoff; Merck).

For further purification, the protein solution was loaded onto a HiLoad 16/600 Superdex 200 column (Cytiva) equilibrated with gel-filtration buffer (25 m*M* Tris–HCl pH 8.0, 0.1 *M* NaCl). MBP–Mb-P′ eluted as a single peak corresponding to the monomer (∼53.8 kDa). The purified protein was concentrated to 16.4 mg ml^{-1} using Amicon Ultra-15 centrifugal filters, flash-cooled in liquid nitrogen and stored at −80°C until use. Macromolecule-production information is summarized in Table 1.

2.2. Crystallization

HPPU ($C_{13}H_{12}N_2O_2$; molecular weight 228.25 Da) was synthesized in-house for this study and its identity was confirmed by NMR. Initial co-crystallization screening of HPPU with the proteins Mb-P′-1 and Mb-P′-2 was performed at 293 K using the sitting-drop vapor-diffusion method with various commercial screening kits. Crystals were obtained under several polyethylene glycol (PEG)-containing conditions. To optimize ligand binding to the proteins, additional crystallization trials were conducted with varying concentrations of HPPU added to the protein solutions. Based on the initial screening results, the precipitant concentration, pH and protein-to-reservoir ratio were systematically optimized. The final crystallization condition consisted of protein solutions containing equimolar HPPU and 20 m*M* maltose combined with reservoir solution composed of 20%(*w*/*v*) PEG 4000, 0.1 *M* sodium acetate, 0.28 *M* ammonium sulfate. Thin plate-like single crystals with typical dimensions of approximately 0.2 × 0.1 × 0.05 mm grew reproducibly within 5–7 days. For cryoprotection, crystals were transferred stepwise into solutions containing gradually increasing concentrations of PEG 4000 from 20 to 30%(*w*/*v*), 0.1 *M* sodium acetate, 0.28 *M* ammonium sulfate, 0.1 m*M* HPPU and 20 m*M* maltose and then flash-cooled in a nitrogen-gas stream at 100 K. Crystallization information is summarized in Table 2.

Table 2
Crystallization of Mb-P′-1.

Method	Vapor diffusion, sitting drop
Plate type	Cryschem M plate (Hampton Research)
Temperature (K)	293
Protein concentration (mg ml^{-1})	16.4
Buffer composition of protein solution	25 m*M* Tris–HCl pH 8.0, 0.1 *M* NaCl, 0.3 m*M* HPPU, 20 m*M* maltose
Composition of reservoir solution	20%(*w*/*v*) PEG 4000, 0.1 *M* sodium acetate, 0.28 *M* ammonium sulfate
Volume and ratio of drop	1 µl protein:1 µl reservoir (1:1)
Volume of reservoir (µl)	500

2.3. Data collection and processing

Crystals obtained from initial screening were evaluated on beamline BL26B1 at SPring-8, Hyogo, Japan using the *in situ* diffraction experiment system (Okumura *et al.*, 2022). The crystallization plate was mounted on a plate gripper attached to the goniometer. To minimize X-ray absorption, the sealing tape covering the wells was replaced with X-ray-transparent film. Diffraction data were collected at a wavelength of 1.0000 Å with an oscillation angle of 0.1° and an exposure time of 1 min per frame.

X-ray diffraction data were collected from an optimized Mb-P′-1 crystal on beamline BL32XU at SPring-8, Hyogo, Japan at a wavelength of 1.0000 Å. Diffraction images were recorded under cryogenic conditions and data sets were automatically indexed, integrated and scaled using the *KAMO* pipeline (Yamashita *et al.*, 2018) implemented in the *ZOO*

Table 3
Data collection and processing.

Values in parentheses are for the outer shell.

Diffraction source	BL32XU, SPring-8
Wavelength (Å)	1.0000
Temperature (K)	100
Detector	EIGER 9M
Crystal-to-detector distance (mm)	310
Rotation range per image (°)	0.1
Total rotation range (°)	360
Exposure time per image (s)	0.02
Space group	$C222_1$
a, b, c (Å)	99.16, 170.58, 422.18
α, β, γ (°)	90, 90, 90
Mosaicity (°)	0.095
Resolution range (Å)	49.3–2.57 (2.66–2.57)
Total No. of reflections	1521444 (118904)
No. of unique reflections	219780 (21765)
Completeness (%)	99.81 (98.36)
Multiplicity	6.92 (5.46)
$\langle I/\sigma(I)\rangle$	9.3 (1.1)
$R_{\rm r.i.m.}$	0.148 (1.359)
$CC_{1/2}$ (%)	99.6 (54.8)
Overall B factor from Wilson plot (Å^2)	64.94

Table 4
Structure refinement.

Values in parentheses are for the outer shell.

Resolution range (Å)	49.3–2.57 (2.60–2.57)
Completeness (%)	99.68 (93.33)
No. of reflections, working set	108113 (3425)
No. of reflections, test set	5597 (155)
Final $R_{\rm cryst}$ (%)	19.56 (44.04)
Final $R_{\rm free}$ (%)	23.33 (47.19)
No. of non-H atoms	
Protein	21250
Ligand (HPPU)	102
Other ligands (maltose, PEG, acetate)	268
Water	336
Total	22956
R.m.s. deviations	
Bond lengths (Å)	0.002
Angles (°)	0.526
Average B factors (Å^2)	
Protein	71.84
Ligand (HPPU)	54.35
Other ligands (maltose, PEG, acetate)	65.33
Water	60.57
Ramachandran plot	
Favored regions (%)	98.67
Additionally allowed (%)	1.33
Outliers (%)	0

system (Hirata *et al.*, 2019). Data-collection and processing statistics are summarized in Table 3. The low-resolution cutoff was set to the lowest resolution limit of the measured data, as the low-resolution reflections exhibit high data quality, with lowest resolution shell statistics of $R_{\rm meas}$ = 0.070, $\langle I/\sigma(I)\rangle$ = 23.6, $CC_{1/2}$ = 0.997 and completeness = 99.9%, and are consistent with stable overall scaling and refinement.

2.4. Structure solution and refinement

The structure of Mb-P′-1 in complex with HPPU was determined by molecular replacement with *MOLREP* (Vagin & Teplyakov, 2010) using the crystal structure of MBP (PDB entry 1y4c; LaPorte *et al.*, 2005) and an *AlphaFold*2-predicted model of apo Mb-P′ as search models. Initial refinement was carried out using *REFMAC*5 (Murshudov *et al.*, 2011). Manual model building was performed with *Coot* (Emsley *et al.*, 2010), and iterative refinement was performed with *phenix.refine* (Afonine *et al.*, 2012) in the *Phenix* suite (Liebschner *et al.*, 2019). After refinement of the apo model, HPPU molecules were modeled into the binding sites and the Mb-P′-1–HPPU complex was further refined with *phenix.refine*. Considering the ionization properties of the phenolic and urea functional groups, HPPU is expected to be predominantly neutral under the crystallization conditions (pH 8.0) and was therefore modeled in its neutral form. The molecular model of HPPU was generated using *Chem3D* (ChemOffice) and stereochemical restraints were prepared with *eLBOW* (Moriarty *et al.*, 2009). Water molecules were added in the final stages of refinement and retained only when supported by $2mF_{\rm o} - DF_{\rm c}$ density ($\geq 1.0\sigma$) and when forming chemically reasonable hydrogen-bonding interactions. Ligand placement was evaluated using polder omit maps calculated with *phenix.polder* (Liebschner *et al.*, 2017); ligand occupancies were tested by group occupancy refinement but were fixed at 1.0 in the final model because the refined values were close to unity and did not improve $R_{\rm work}/R_{\rm free}$. Structural figures were prepared using *PyMOL* (version 3.1.0; Schrödinger) and *UCSF ChimeraX* (version 1.9; Meng *et al.*, 2023). Refinement statistics are summarized in Table 4.

3. Results and discussion

3.1. Protein expression and purification

Initial expression of Mb-P′ with an N-terminal His_6 tag in *E. coli* yielded sufficient protein for purification by Ni^{2+}-affinity chromatography and extensive crystallization screening. However, analytical size-exclusion chromatography revealed severe polydispersity: the protein eluted over a broad range of volumes, consistent with heterogeneous oligomerization and/or aggregation rather than a single well defined form. To improve solubility and monodispersity, we adopted an MBP fusion strategy. Two MBP–Mb-P′ fusion constructs carrying different linkers (NAAATGS, designated Mb-P′-1, and TSGTGS, designated Mb-P′-2) were generated and expressed in *E. coli*. Both fusion constructs were produced at high levels (>30 mg of purified protein per litre of culture). Analytical size-exclusion chromatography showed a marked improvement in sample homogeneity for both fusion proteins, with single, symmetric peaks eluting at volumes corresponding to MBP–monobody monomers (calculated molecular mass of 53.8 kDa), although minor oligomeric peaks were occasionally observed for Mb-P′-1 (Fig. 2*b*). Given the substantial improvement in monodispersity achieved with both fusion proteins, parallel crystallization trials were conducted with both constructs.

3.2. Crystallization and data collection

Initial co-crystallization screening of the MBP–Mb-P′ fusion proteins was performed using sitting-drop vapor

diffusion with commercial sparse-matrix screens. To identify the optimal linker configuration for structural analysis, crystallization conditions were explored for both Mb-P′-1 and Mb-P′-2. Crystals were obtained under several conditions for both constructs, with Mb-P′-1 yielding crystallization hits at a higher frequency than Mb-P′-2. To evaluate the diffraction quality of the initial crystals while avoiding potential damage from crystal harvesting or cryoprotection, we employed the *in situ* diffraction measurement system installed at SPring-8 beamline BL26B1. Crystals were grown in standard 96-well polystyrene crystallization plates (not specifically designed for *in situ* diffraction experiments) and directly exposed to X-rays. The plate-scan results consistently showed that Mb-P′-1 produced crystals that diffracted to slightly higher resolution than those from Mb-P′-2 (Fig. 3*a*). Consequently, Mb-P′-1 was selected for further optimization. Systematic refinement of the precipitant concentration, pH and protein-to-reservoir ratio resulted in the reproducible growth of thin plate-like single crystals with typical dimensions of approximately 0.2 × 0.1 × 0.05 mm within 5–7 days at 293 K. For final data collection, crystals were transferred stepwise to solutions containing gradually increasing concentrations of PEG 4000 from 20 to 30%(*w*/*v*) in the presence of 0.1 m*M* HPPU for cryoprotection and then flash-cooled in a nitrogen-gas stream at 100 K. The crystals diffracted to a maximum resolution of 2.57 Å and belonged to space group $C222_1$, with unit-cell parameters a = 99.16, b = 170.6, c = 422.2 Å (Table 3). Due to the large unit-cell dimension along the c axis, data collection was performed at the maximum available detector distance to minimize spot overlap and ensure the accurate integration of reflections (Fig. 3*b*).

3.3. Structure determination and packing analysis

Molecular replacement was successfully performed using the crystal structure of MBP together with an *AlphaFold*2-predicted structural model of Mb-P′ as search templates. Six MBP–Mb-P′ fusion molecules were found in the asymmetric unit, adopting a pseudo-D_3 arrangement. After refinement, the final electron-density maps showed well resolved features for both the MBP and Mb-P′ domains, facilitating reliable model building.

The refined asymmetric unit contents are shown in Fig. 4(*a*). To assess the quality of the pseudo-D_3 arrangement, pairwise superposition of the pseudo-C_2-related dimers in the refined model yielded low r.m.s.d. values (0.46–0.86 Å), indicating that the dimeric substructures are well conserved (Supplementary Fig. 1*a*). In contrast, superpositions of the pseudo-C_3-related trimers showed substantially larger deviations (r.m.s.d. of 2.77 Å), demonstrating that the overall D_3 symmetry is only approximate and is partially broken (Supplementary Fig. 1*b*). The MBP domains cluster around the noncrystallographic threefold axis in two tiers of three molecules each, whereas the monobody domains align along the noncrystallographic twofold axes to form a staggered array. Each monobody interacts with two neighboring monobodies through distinct interfaces: one primarily involving FG–FG loop contacts and the other mediated by multiple regions including the BC and

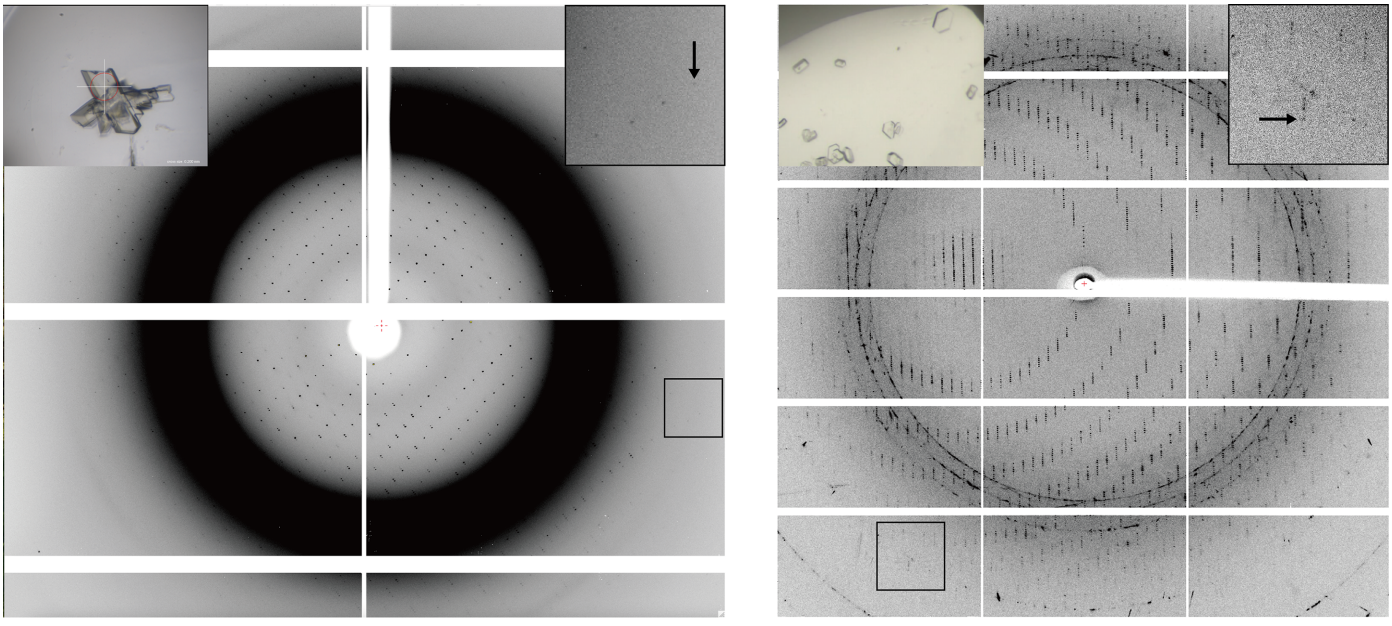

(*a*) (*b*)

Figure 3
X-ray diffraction images of Mb-P′-1 crystals. (*a*) A representative diffraction image obtained from an *in situ* diffraction experiment; the highest resolution reflections extend to 3.5 Å resolution (arrow). (*b*) Diffraction image collected from the crystal used for structure determination and refinement, showing reflections to 2.57 Å resolution (arrow). For each panel, a photograph of the corresponding crystal is shown in the upper left inset and an enlarged view around the highest resolution reflections is shown on the right. The enlarged region is indicated by a black box on the diffraction image.

FG loops. In addition, each monobody is closely surrounded by its own MBP moiety and by two adjacent MBP molecules, creating an isolated local environment. Monobody–monobody contacts are confined within the asymmetric units; interactions between neighboring asymmetric units are mediated exclusively by MBP.

When expressed alone, Mb-P′ formed heterogeneous oligomeric species, whereas N-terminal fusion with MBP effectively suppressed oligomerization. Superposition of the six MBP–Mb-P′ molecules in the refined asymmetric unit revealed pairwise r.m.s.d. values of 0.23–0.58 Å, demonstrating that the relative orientation of the MBP and monobody domains is highly conserved. These observations suggest that MBP fusion restricts the rotational and conformational freedom of the monobody domain, thereby preventing the aggregation that would occur in the absence of the fusion partner. In the crystal structure, the MBP moiety interacts with and partially covers the F and G β-strands of Mb-P′ (Figs. 4*b* and 4*c*). This structural arrangement suggests that MBP sterically shields surfaces that would otherwise drive oligomer formation.

A previous study of an MBP-fused monobody reported a distinctly different domain arrangement in which the FG loop of the monobody was oriented away from the fused MBP (Koide *et al.*, 2007). However, because that monobody was specifically selected to recognize MBP, the observed arrangement was dictated by crystal packing mediated by intermolecular antigen–antibody interactions rather than representing an intrinsic property of the fusion. Consequently, that study offers limited insight into the general influence of MBP on monobody oligomerization. In contrast, our structure reveals an intramolecular arrangement where MBP directly engages the F and G β-strands of Mb-P′, providing a plausible structural basis for the suppression of aggregation. While compelling, this model warrants further validation, as the specific effects of mutations on strands F and G have not yet been experimentally examined.

Well defined positive electron density corresponding to the HPPU ligand was clearly identified in the polder omit map contoured at 5.0σ (Fig. 5). The density exhibits an elongated shape matching the molecular geometry of HPPU. Although HPPU is nearly symmetric, a subtle but distinct protrusion

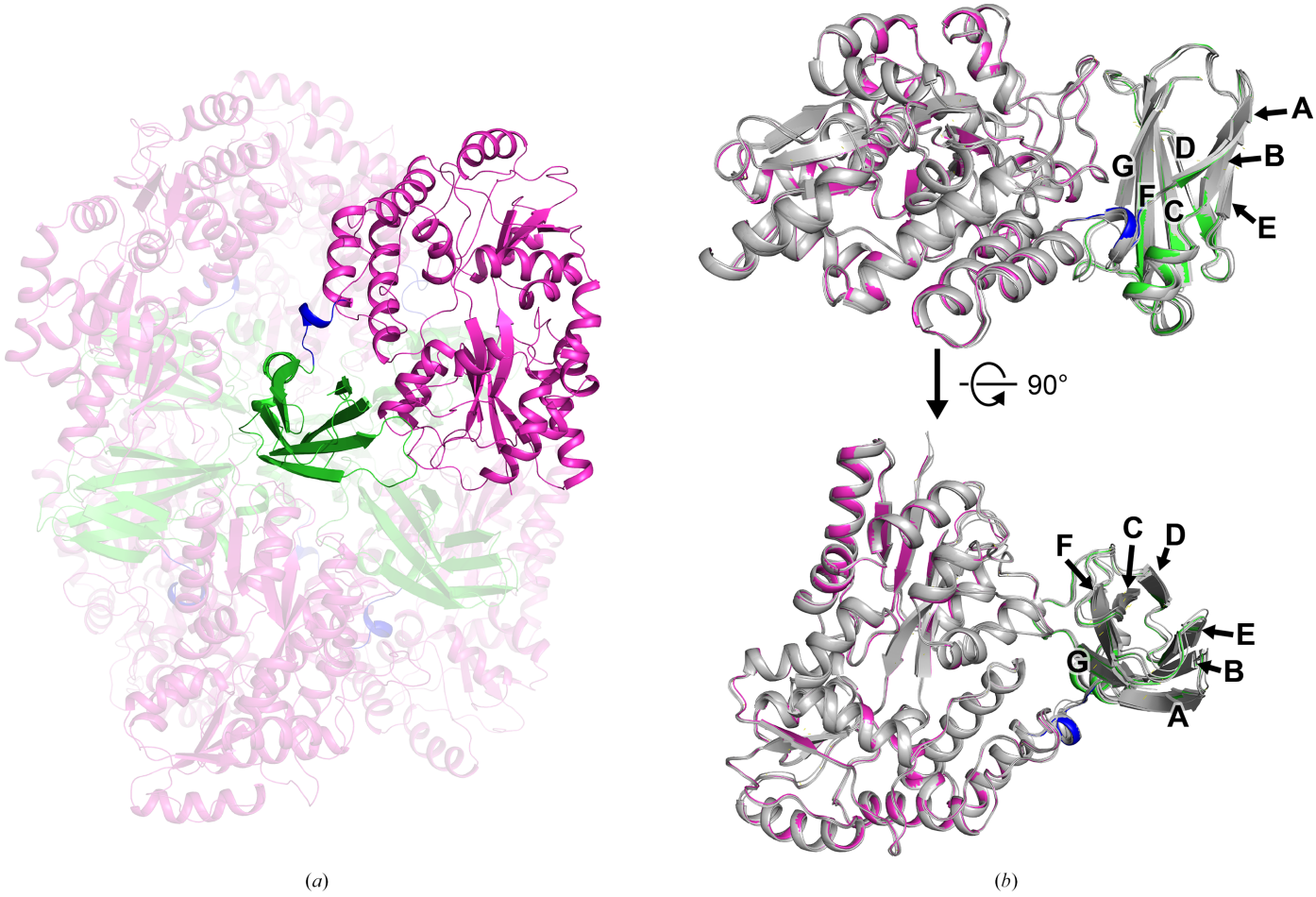

(*a*) (*b*)

Figure 4
Structure of Mb-P′-1 fusion proteins in the asymmetric unit. (*a*) Overall arrangement of the six molecules in the asymmetric unit. Molecules are colored by region: the MBP domain is magenta, the linker region is blue and the Mb-P′ domain is green. One representative molecule is shown in solid representation, while the others are rendered semi-transparently for clarity. (*b*) Superposition of the six molecules. The representative molecule is colored as in (*a*) with Mb-P′ β-strands labeled A–G, while others are shown in gray to demonstrate the conserved relative domain orientation.

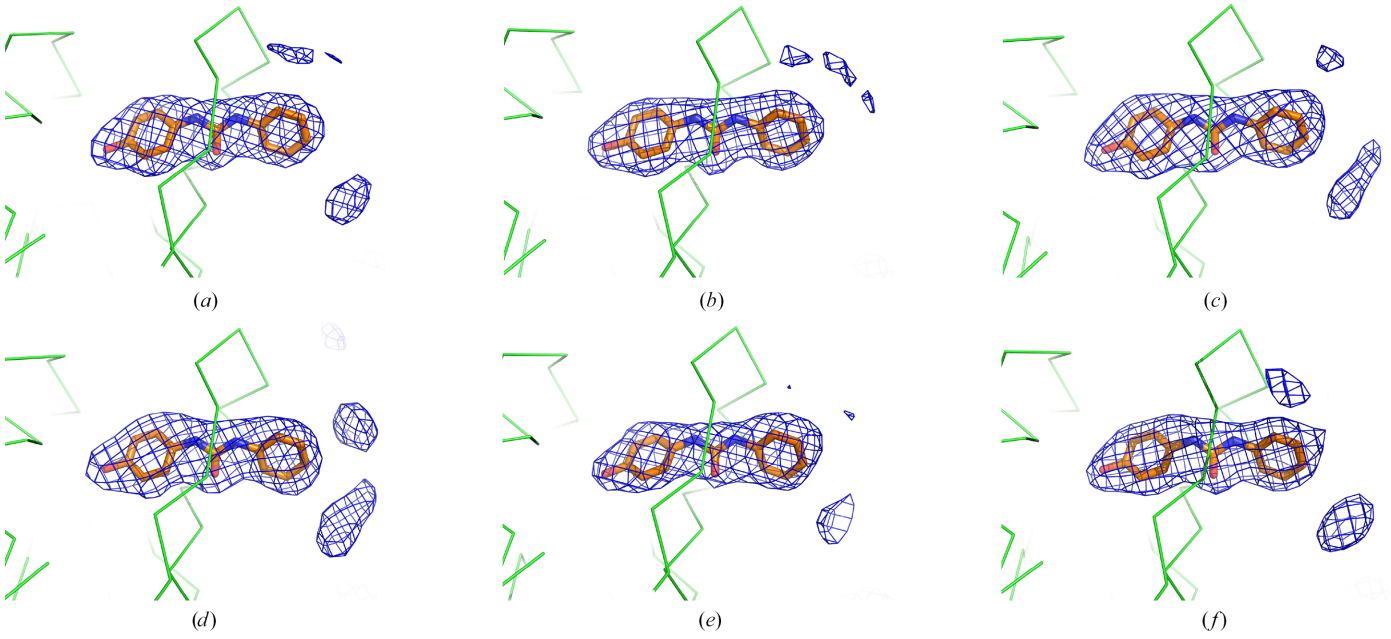

Figure 5
Polder omit maps of the bound HPPU ligand in all chains of the asymmetric unit. Polder omit electron-density maps (blue mesh), contoured at 5.0σ, are shown for HPPU in chains *A*–*F* of the asymmetric unit in (*a*)–(*f*), respectively. HPPU is shown as an orange stick model and the Mb-P′ backbone as a green ribbon. The clear density features allow unambiguous assignment of the ligand orientation in each chain.

corresponding to the hydroxyl substituent allowed the unambiguous assignment of the ligand orientation. In addition, a protrusion evident in the central region is consistent with the urea carbonyl oxygen. A detailed analysis of the protein–ligand interactions is the subject of a separate manuscript currently in preparation.

Notably, the HPPU in chain *E* exhibits higher *B* factors (76.4 Å^2) than those in the other chains (45.6–54.3 Å^2; Supplementary Table S1), mirroring the elevated *B* factor of the corresponding monobody domain in the same chain (87.1 Å^2 versus 61.8–74.2 Å^2 for the other chains). This chain-to-chain heterogeneity is also apparent in the *B*-factor-colored packing diagrams and cartoon putty representations (Supplementary Figs. S2*a* and S2*b*), consistent with *B* factors varying with the local packing environment. We therefore interpret the higher ligand *B* factors in chain *E* as reflecting chain-specific packing heterogeneity rather than differences in ligand-binding geometry.

4. Conclusions

The successful crystallization of the MBP–Mb-P′ fusion protein highlights the utility of this approach for overcoming the aggregation issues that are often encountered during the production of monobodies. The MBP fusion tag not only stabilized the protein in solution but also facilitated the formation of well ordered crystals suitable for high-resolution structural analysis. Our structural data suggest that this stabilization is mediated by steric shielding of the aggregation-prone FG region by the MBP domain, although further mutational studies would be required to strictly confirm this mechanism. Consequently, this strategy offers a promising template applicable to other challenging monobody targets where aggregation hinders structural characterization.

Acknowledgements

The synchrotron-radiation experiments were performed on BL26B1 and BL32XU at SPring-8 with the approval of the Japan Synchrotron Radiation Research Institute (JASRI; Proposal Nos. 2022A2756 and 2022B2756). We thank the beamline scientists at beamlines BL26B1 and BL32XU of SPring-8 for their help with X-ray diffraction data collection.

Funding information

Funding for this research was provided by: Japan Society for the Promotion of Science (grant No. JP22H04753 to Tomoya Hino); Japan Society for the Promotion of Science (grant No. 23H05456 to Hiroshi Murakami).

References

Afonine, P. V., Grosse-Kunstleve, R. W., Echols, N., Headd, J. J., Moriarty, N. W., Mustyakimov, M., Terwilliger, T. C., Urzhumtsev, A., Zwart, P. H. & Adams, P. D. (2012). *Acta Cryst.* D**68**, 352–367.
Batori, V., Koide, A. & Koide, S. (2002). *Protein Eng. Des. Sel.* **15**, 1015–1020.
Bever, C. S., Dong, J. X., Vasylieva, N., Barnych, B., Cui, Y., Xu, Z. L., Hammock, B. D. & Gee, S. J. (2016). *Anal. Bioanal. Chem.* **408**, 5985–6002.
Binz, H. K., Amstutz, P., Kohl, A., Stumpp, M. T., Briand, C., Forrer, P., Grütter, M. G. & Plückthun, A. (2004). *Nat. Biotechnol.* **22**, 575–582.
Binz, H. K., Stumpp, M. T., Forrer, P., Amstutz, P. & Plückthun, A. (2003). *J. Mol. Biol.* **332**, 489–503.

Center, R. J., Kobe, B., Wilson, K. A., Teh, T., Kemp, B. E., Poumbourios, P. & Howlett, G. J. (1998). *Protein Sci.* **7**, 1612–1619.
Emsley, P., Lohkamp, B., Scott, W. G. & Cowtan, K. (2010). *Acta Cryst.* D**66**, 486–501.
Hamers-Casterman, C., Atarhouch, T., Muyldermans, S., Robinson, G., Hammers, C., Songa, E. B., Bendahman, N. & Hammers, R. (1993). *Nature*, **363**, 446–448.
Hirata, K., Yamashita, K., Ueno, G., Kawano, Y., Hasegawa, K., Kumasaka, T. & Yamamoto, M. (2019). *Acta Cryst.* D**75**, 138–150.
Ishizawa, T., Kawakami, T., Reid, P. C. & Murakami, H. (2013). *J. Am. Chem. Soc.* **135**, 5433–5440.
Koide, A., Bailey, C. W., Huang, X. & Koide, S. (1998). *J. Mol. Biol.* **284**, 1141–1151.
Koide, A., Gilbreth, R. N., Esaki, K., Tereshko, V. & Koide, S. (2007). *Proc. Natl Acad. Sci. USA*, **104**, 6632–6637.
Koide, A., Wojcik, J., Gilbreth, R. N., Hoey, R. J. & Koide, S. (2012). *J. Mol. Biol.* **415**, 393–405.
Kondo, T., Eguchi, M., Kito, S., Fujino, T., Hayashi, G. & Murakami, H. (2021). *Chem. Commun.* **57**, 2416–2419.
LaPorte, S. L., Forsyth, C. M., Cunningham, B. C., Miercke, L. J., Akhavan, D. & Stroud, R. M. (2005). *Proc. Natl Acad. Sci. USA*, **102**, 1889–1894.
Liebschner, D., Afonine, P. V., Baker, M. L., Bunkóczi, G., Chen, V. B., Croll, T. I., Hintze, B., Hung, L.-W., Jain, S., McCoy, A. J., Moriarty, N. W., Oeffner, R. D., Poon, B. K., Prisant, M. G., Read, R. J., Richardson, J. S., Richardson, D. C., Sammito, M. D., Sobolev, O. V., Stockwell, D. H., Terwilliger, T. C., Urzhumtsev, A. G., Videau, L. L., Williams, C. J. & Adams, P. D. (2019). *Acta Cryst.* D**75**, 861–877.
Liebschner, D., Afonine, P. V., Moriarty, N. W., Poon, B. K., Sobolev, O. V., Terwilliger, T. C. & Adams, P. D. (2017). *Acta Cryst.* D**73**, 148–157.
Meng, E. C., Goddard, T. D., Pettersen, E. F., Couch, G. S., Pearson, Z. J., Morris, J. H. & Ferrin, T. E. (2023). *Protein Sci.* **32**, e4792.
Moriarty, N. W., Grosse-Kunstleve, R. W. & Adams, P. D. (2009). *Acta Cryst.* D**65**, 1074–1080.
Murshudov, G. N., Skubák, P., Lebedev, A. A., Pannu, N. S., Steiner, R. A., Nicholls, R. A., Winn, M. D., Long, F. & Vagin, A. A. (2011). *Acta Cryst.* D**67**, 355–367.
Muyldermans, S., Atarhouch, T., Saldanha, J., Barbosa, J. A. & Hamers, R. (1994). *Protein Eng. Des. Sel.* **7**, 1129–1135.
Okumura, H., Sakai, N., Murakami, H., Mizuno, N., Nakamura, Y., Ueno, G., Masunaga, T., Kawamura, T., Baba, S., Hasegawa, K., Yamamoto, M. & Kumasaka, T. (2022). *Acta Cryst.* F**78**, 241–251.
Vagin, A. & Teplyakov, A. (2010). *Acta Cryst.* D**66**, 22–25.
Waugh, D. S. (2016). *Protein Sci.* **25**, 559–571.
Yamashita, K., Hirata, K. & Yamamoto, M. (2018). *Acta Cryst.* D**74**, 441–449.